ADVANCING EARTH AND SPACE SCIENCES

Earth and Space Science

RESEARCH ARTICLE
10.1029/2025EA004901

Special Collection:
TEMPO Data Products, Science, and Applications

Key Points:

- Developed two complementary correction methods for TEMPO twilight data, which together yield more stable and reliable corrections
- Corrected TEMPO data reproduce urban light patterns consistent with VIIRS Black Marble
- TEMPO closely matches ISS nighttime spectral signatures in bright urban cores and major roads

Supporting Information:
Supporting Information may be found in the online version of this article.

Correspondence to:
J. Wang and M. Zhou,
jun-wang-1@uiowa.edu;
meng-zhou-1@uiowa.edu

Citation:
Xue, Z., Zhou, M., Wang, J., Xiao, Q., Carr, J., Liu, X., et al. (2026). Spectral-resolved light at night: TEMPO observations and background correction. *Earth and Space Science*, *13*, e2025EA004901. https://doi.org/10.1029/2025EA004901

Received 12 NOV 2025
Accepted 23 MAY 2026

Author Contributions:
Conceptualization: Zhixin Xue, Meng Zhou, Jun Wang
Formal analysis: Zhixin Xue
Funding acquisition: Jun Wang
Investigation: Zhixin Xue, Meng Zhou, Jun Wang
Methodology: Zhixin Xue
Software: Zhixin Xue
Writing – review & editing: Meng Zhou, Jun Wang, Qian Xiao, Jim Carr, Xiong Liu, Heesung Chong, John Houck

Spectral-Resolved Light at Night: TEMPO Observations and Background Correction

Zhixin Xue[1], Meng Zhou[1,2,3], Jun Wang[1], Qian Xiao[4], Jim Carr[5], Xiong Liu[6], Heesung Chong[6], and John Houck[6]

[1]Department of Chemical and Biochemical Engineering, The University of Iowa, Iowa City, IA, USA, [2]Goddard Earth Sciences Technology and Research II, University of Maryland, Iowa city, MD, USA, [3]Global Modeling and Assimilation Office (GMAO), NASA Goddard Space Flight Center, Greenbelt, MD, USA, [4]Department of Epidemiology, Human Genetics and Environmental Sciences, School of Public Health, The University of Texas Health Science Center at Houston, Houston, TX, USA, [5]Carr Astronautics, Greenbelt, MD, USA, [6]Atomic and Molecular Physics Division, Center for Astrophysics | Harvard Smithsonian, Cambridge, MA, USA

Abstract Artificial Light at Night (ALAN) poses risks to public health and ecosystems. While long-term remote sensing has tracked global nighttime light, spectrally resolved light at night (spectral light at night (SLAN)) data from geostationary orbit only became available with NASA's Tropospheric Emissions: Monitoring of Pollution (TEMPO) mission. Its Level 1 twilight radiance product enables detailed spatiotemporal analysis of ALAN's spectral characteristics. This study introduces algorithms for processing TEMPO Level 1 data into Level 2 SLAN data using two methods for solar background removal: scattering-angle correction and spectral correction. The first method uses the relationship between scattering angle and radiance to suppress background, while the second uses the inherent spectral relations in the solar radiation in 290–390 nm range, where artificial light emissions are minimized, to estimate direct twilight contributions. Combined, these methods yield more stable correction results. The results are validated against two independent data sets: the Visible Infrared Imaging Radiometer Suite (VIIRS) Day/Night Band (DNB) Black Marble product and astronaut photographs taken from the International Space Station (ISS) over Houston. Comparisons include (a) city light classifications from Black Marble versus both raw and corrected TEMPO data, (b) pixel-to-pixel radiance measurements between TEMPO and VIIRS, and (c) spectral angle analyses between ISS and TEMPO data. We also compare CONUS nighttime light maps from VIIRS DNB, TEMPO VIS, and TEMPO UV; TEMPO VIS agrees closely with VIIRS DNB, while both diverge from TEMPO UV in gas-flaring regions, highlighting the complementary information these instruments provide.

Plain Language Summary Artificial Light at Night harms ecosystems and human health. Blue light, in particular, disrupts sleep and circadian rhythms, which is linked to problems like cancer, diabetes, heart disease, and obesity. Most satellites have only measured how bright city lights are; NASA's TEMPO mission also measures their color. We created a method to clean TEMPO's raw data by removing solar background, giving clearer views of both color and brightness. The results match independent light maps from other satellite product and photos from the ISS, especially in city centers and along major roads, opening new ways to study light pollution.

1. Introduction

Understanding and characterizing the spectral properties of nighttime artificial lighting is critical, especially given biological sensitivities to short-wavelength illumination, including UV wavelengths, among almost all species on Earth. The increasing prevalence of artificial lighting has raised concerns about its widespread environmental and physiological effects. With the widespread use of electric-powered light sources, Artificial Light at Night (ALAN) originates from various point sources, including municipal, industrial, commercial, and residential lighting (Davies & Smyth, 2018). There is growing interest in studying the ecological and health impacts of ALAN due to its widespread global distribution and its numerous environmental and public health consequences (Davies & Smyth, 2018; Gaston et al., 2017; Gaston & Sánchez de Miguel, 2022; Song et al., 2021). Artificial Light at Night alters organism physiology, reshapes ecological community structures, and affects numerous species by disrupting animal communication, reproduction, orientation, habitat selection, predator avoidance, predation pressure, circadian rhythms, plant phenology, and ecosystem services (Bennie et al., 2016; Bolton

10.1029/2025EA004901

et al., 2017; Davies & Smyth, 2018; Davies et al., 2015; Dominoni et al., 2013; Frank, 1988; Knop et al., 2017; Raap et al., 2015; van Geffen et al., 2015; Wakefield et al., 2015). Among various light sources, Light-emitting diode (LEDs) have become increasingly dominant due to their energy efficiency (Wang et al., 2020; Zissis et al., 2021). However, their strong short-wavelength emissions coincide with the spectral range where the circadian response to light peaks among most living organisms, including humans (Davies et al., 2013). White LEDs, in particular, can alter species interactions and trigger attraction or disorientation responses in species such as seabirds (Davies et al., 2013; Middlemiss et al., 2025). Moreover, higher correlated color temperatures and increased illuminance levels in the evening from white LEDs have been found to strongly suppress melatonin, potentially desynchronizing circadian rhythms and negatively affecting sleepiness, cognitive performance, and visual comfort (Rea et al., 2012; Stefani et al., 2021).

Satellite-based remote sensing provides a powerful tool for large-scale monitoring of ALAN. Outdoor ALAN can be estimated through various methods, including field measurements using illuminometers, satellite-observed artificial sky brightness, and self-reported questionnaires (Wang et al., 2023). However, satellite data remains the most effective approach, enabling the capture of the global distribution of city lights and the creation of a comprehensive outdoor ALAN world atlas (Cinzano et al., 2001). The first world atlas of ALAN was generated using data from the Defense Meteorological Satellite Program (DMSP) Operational Linescan System (Cinzano et al., 2001). This was later refined using the Visible Infrared Imaging Radiometer Suite (VIIRS) Day/Night Band (DNB) aboard the Suomi National Polar-orbiting Partnership (Suomi NPP) satellite (Falchi et al., 2016; Zhou et al., 2021, 2024). VIIRS DNB is a panchromatic sensor with high sensitivity to low-light conditions, capturing emissions in the visible and near-infrared spectrum (400–900 nm) at ∼750m resolution (Liao et al., 2013; Zhou et al., 2023). To enhance data quality and produce clear radiance maps, the Black Marble algorithm include corrections for cloud cover, atmospheric interference, terrain variations, vegetations, snow, lunar illumination and stray light (Mills et al., 2013; Román et al., 2018a, Román et al., 2018a). These data sets enable researchers to analyze spatial patterns and temporal trends in ALAN (Xiao, Lyu, et al., 2023; Xiao, Zhou, et al., 2023). Despite these research advances, lack of spectral resolution in previous satellite data sources has limited the ability to fully understand the ecological and health effects of ALAN.

To provide the spectral detail (or light color information) missing from Black Marble, this study uses TEMPO twilight observations to deliver high-resolution nighttime ALAN spectra. TEMPO, part of NASA's Earth Venture Instrument program, primarily measures trace gases and aerosols affecting air quality over North America (Naeger et al., 2021; Zoogman et al., 2017). Since August 2023, it has been collecting spectral data in the 293–494 nm and 538–741 nm ranges, with a spectral resolution of 0.6 nm (spectral interval of 0.2 nm) and a spatial resolution of ∼4.75 km (E/W) × 2 km (N/S) (Zoogman et al., 2017). Although TEMPO was designed for daytime atmospheric monitoring, its twilight radiance product provides a unique opportunity for ALAN studies by capturing nighttime light spectra only when the Sun is >60° from its boresight to avoid instrument damage (Carr et al., 2017; Zoogman et al., 2017). Its fine spectral resolution allows researchers to distinguish different light sources, including LEDs and fluorescent lights, improving the accuracy of urban light pollution assessments (Carr et al., 2017, 2025; Wang et al., 2016). In addition, twilight observations can capture stronger artificial light signals associated with higher human activity during late evening and early morning periods, compared to late-night observations such as those from VIIRS-DNB.

Because TEMPO is a new source of ALAN information and its twilight observations can be contaminated by solar background signals (Carr et al., 2025), we here develop the methods to remove the background signal to generate spectral light at night (SLAN) data product that can be used in future to study artificial light pollution. Section 2 introduces the data sets used and Section 3 details two background correction methods, documenting step-by-step refinements to produce a corrected TEMPO product. Section 4 evaluates this corrected product against the reference data sets over the Houston metropolitan area to assess spatial and spectral consistency.

2. Data Sets

To process the TEMPO twilight data set for its application in circadian light studies in clear sky conditions, we use the geostationary GOES clear sky mask product to filter out TEMPO's cloudy pixels. We then compare the TEMPO data set with VIIRS Black Marble and ISS astronaut photography. Table S1 in Supporting Information S1 summarizes the key characteristics of each data set, including spectral coverage and spatial resolution. The following subsections provide a detailed description of each data set.

10.1029/2025EA004901

2.1. TEMPO Twilight Measurements

TEMPO is an imaging spectrometer that captures both UV and visible spectra at a spatial resolution of 2 km × 4.75 km at the center of the field of regard. During its scanning, light reflected off the scan mirror is directed onto the entrance slit of an Offner-type spectrometer, where it is spectrally dispersed onto two CCD (Charged Coupled Device) focal plane arrays (Carr et al., 2017, 2025). One CCD covers wavelengths from 293 to 494 nm in 0.2 nm increments, while the other covers 538–741 nm in the same increments.

The Version 3 TEMPO twilight data (TEMPO_RADT_L1_V03) was used in this study (Chong et al., 2026). Twilight observations are conducted during early morning and late evening at the spacecraft longitude. Morning scans capture nighttime conditions in the western portion of the field of regard, while evening scans capture the eastern portion. Observations are constrained by a solar safety requirement that prohibits aperture opening when the Sun is within 60° of the instrument boresight. As a result, nighttime observation opportunities are longest near the winter solstice and highly limited between May 20 and July 20. To maximize data quality and minimize solar contamination, twilight measurements are primarily scheduled between mid-August and mid-April. The number and duration of scans within each twilight window depend on the time available under safety constraints. When the window is short, fewer or no nighttime scans are performed, and regions may be revisited over multiple days if necessary.

In this study, we use twilight data collected between February 1 and April 25, as well as September 5 and 31 December 2024. Since TEMPO's twilight observation geolocations vary daily, we re-grid all data to a uniform 0.05° grid over CONUS (25°N–50°N, 125°W–60°W).

2.2. GOES Clear Sky Mask

The GOES-16 clear sky mask (ACM) product provides a binary clear-sky mask every five minutes for the CONUS region at a 2 km spatial resolution. To ensure consistency with TEMPO, we re-grid the ACM product to a 0.05° resolution. During nighttime and twilight, visible channels become less useful, so the ACM algorithm relies on six IR channels: 3.9 μm, 7.0 μm, 7.4 μm, 8.5 μm, 11.2 μm, and 12.3 μm (Heidinger, 2011). The nighttime cloud detection accuracy of the ACM is approximately 85.8% when compared with CALIPSO retrievals. This data set is crucial for filtering out cloud-contaminated pixels in the TEMPO twilight data set, ensuring that our analysis focuses on clear-sky conditions.

2.3. VIIRS DNB Black Marble Data Sets

The Black Marble product includes the daily at-sensor top of atmosphere (TOA) nighttime lights (NTL) product (VNP46A1) and daily moonlight-adjusted nighttime lights product (VNP46A2). Both products are provided at a spatial resolution of 500 m. The VNP46A2 product offers daily nighttime light observations based on cloud-free, atmospheric-, terrain-, vegetation-, snow-, lunar-, and stray light-corrected DNB (Day-Night Band) radiances (Román et al., 2018a, Román et al., 2018a). To enhance data accuracy, VNP46A2 applies several correction techniques: (a) Atmospheric correction accounts for the influence of aerosols, water vapor, and ozone on nighttime light radiances; (b) Bidirectional Reflectance Distribution Function (BRDF) correction estimates the contributions of moonlight, aerosols, and surface albedo through an analytical BRDF model inversion; (c) Seasonal correction compensates for seasonal variations in nighttime lights using canopy radiative transfer methods. For consistency across data sets, VIIRS DNB data (VNP46A1 & VNP46A2) are re-gridded to a 0.05° resolution, aligning with that of TEMPO and GOES ACM products. By offering high-quality, cloud-free nighttime observations, VIIRS DNB serves as a valuable reference for evaluating TEMPO's twilight products.

Globally, VIIRS nighttime cloud detection achieves approximately 94% accuracy (Wang et al., 2021). However, quantifying the absolute accuracy of NightTime Lights (NTL) retrievals remains challenging due to the limited availability of spatially and temporally dense, high-quality in situ reference data. Several factors contribute to uncertainties in NTL retrievals, including view-illumination geometry, surface BRDF effects, snow cover, lunar irradiance, aerosol loading, cloud masking accuracy, vegetation structure, and transient or ephemeral artifacts.

2.4. ISS Astronaut Nighttime Photography

Unlike satellite imagery, which follows an automated and precisely controlled acquisition process, ISS astronaut photos are captured using handheld cameras, resulting in greater variability in sensor pose (Stoken &

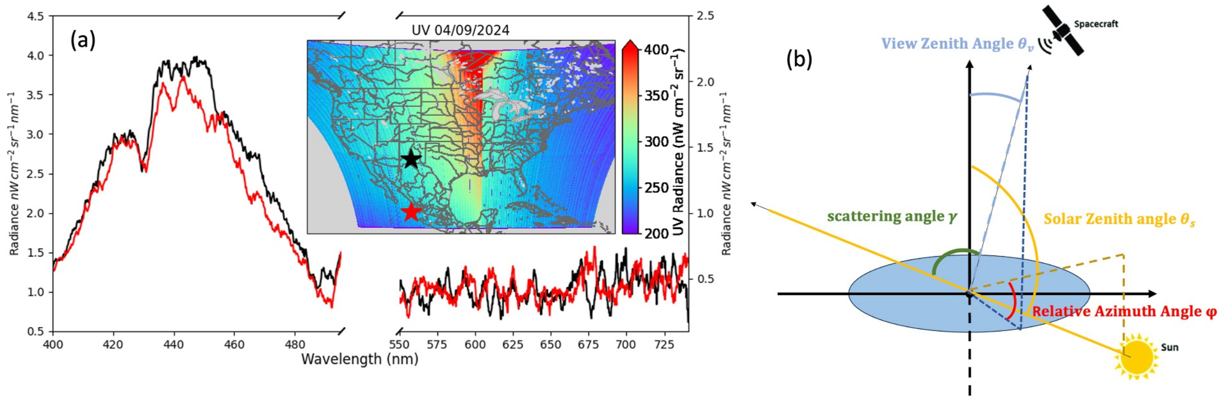

Figure 1. TEMPO raw radiance spectra and scattering geometry. (a) TEMPO radiance spectra at two different locations (red and black lines correspond to locations of the red and black stars shown on the inset map). The inset map displays the spatial distribution of UV radiance (290–490 nm) over North America on 9 April 2024 (exposure time: 3s), highlighting the potential dependence of background radiance on viewing geometry. The black star marks White Sands National Park, and the red star marks a location over the ocean. Both high- and low-albedo surfaces exhibit similar high peaks in the UV range. (b) Schematic illustration of the solar-viewing geometry, defining the solar zenith angle (θ_s), view zenith angle (θ_v), relative azimuth angle (φ), and scattering angle (γ).

Fisher, 2023). As a result, astronaut imagery exhibits a high degree of variability compared to its satellite counterparts. The conditions under which astronauts take these photographs add to the challenge of localization, whether by human analysis or automated methods (Stoken & Fisher, 2023). Imagery taken from the ISS has a high spatial resolution of approximately 20 m. However, the spacecraft's orbit imposes certain limitations, as it does not pass over every point on Earth daily. Although multiple photographs of major U.S. cities such as Houston are taken each year, there is no consistent pattern in the images astronauts choose to capture, resulting in a low and irregular temporal resolution (Johnson, 2020). To facilitate comparison with other data sets, astronaut imagery is manually georeferenced and selected based on its alignment with study regions (Houston region).

3. Methods and Results

3.1. TEMPO Twilight Data Sets Preprocessing

This section introduces two background correction methods. The first method uses the relationship between radiance and scattering angle to correct individually for each spectral line, treating each wavelength as an independent channel. The second method estimates twilight spectrum contribution using measurements in 290–390 nm range and through assumption that this estimate is same across entire TEMPO spectral range, use it for performing the background correction. Both methods yield similar results across most wavelengths, though their performance differ in certain wavelength ranges. The processing time also varies between the two approaches and depends on the available computing resources. In general, the spectral correction method is computationally more intensive than the scattering-angle correction approach because it includes additional spectral fitting and background estimation procedures. In practice, combining the two methods often leads to improved correction accuracy in the final SLAN data product.

3.1.1. Scattering Angle Correction Approach

The TEMPO twilight product often exhibits significant background signal, particularly in the UV channel (293–494 nm), as shown in Figure 1a. The distribution map from 9 April 2024, reveals elevated values over the northern Great Plains region, likely due to high background signals near the terminator. This inference is supported by the spectral characteristics of the background, which closely resemble those of twilight—peaking around 440 nm and showing strong intensity in the UV range (Kelber et al., 2017). To better understand the source of this background and improve data set correction, we investigated the relationship between UV (and visible) radiances and various geometric angles, including solar zenith angle (SZA), view zenith angle (VZA), and relative azimuth angle (RAZ).

Our analysis revealed a notable correlation between background radiances and both the scattering angle and exposure time. Exposure time refers to the duration the detector collects light (photons) for each scan line (or

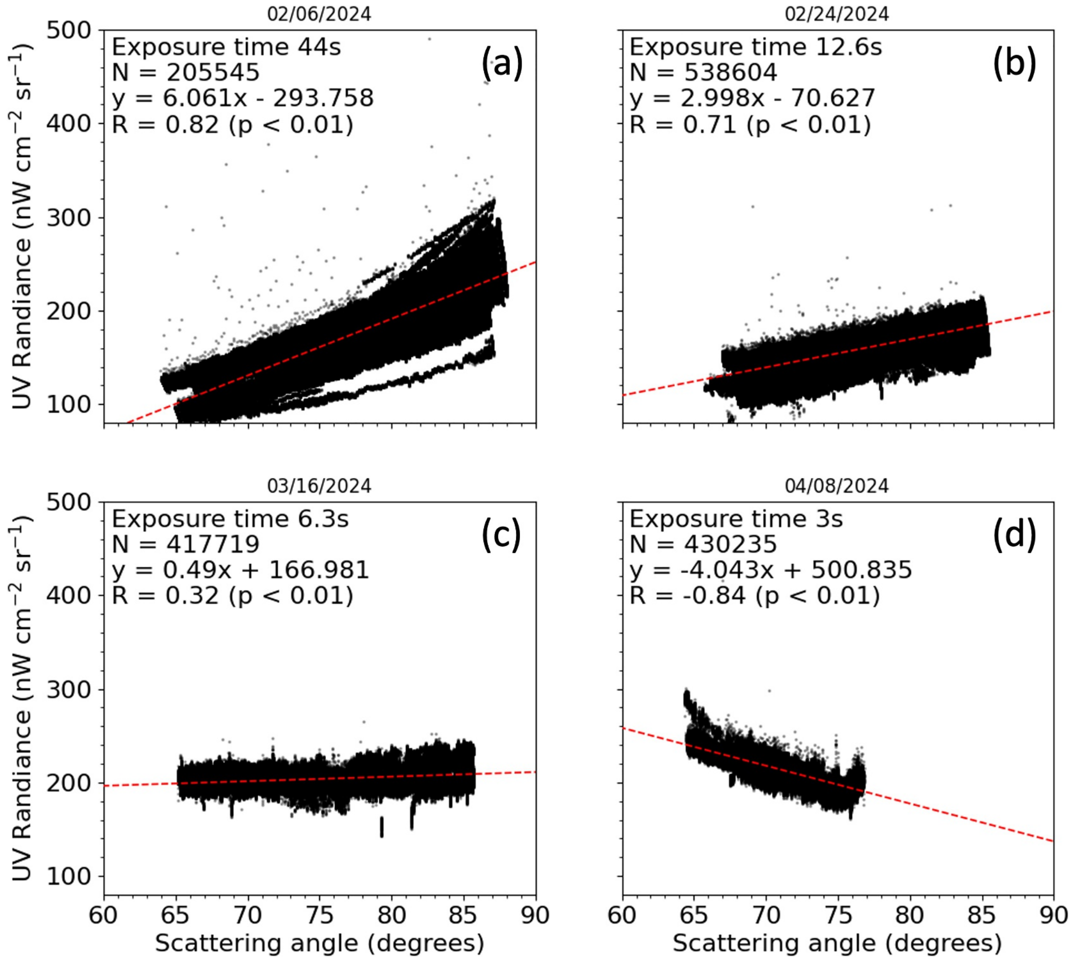

Figure 2. Linear relationship between TEMPO UV radiance (390–490 nm) and scattering angle at 4 selected days with four typical exposure times respectively over the continental United States (CONUS). Pixels with a solar zenith angle (SZA) < 100° are excluded, as radiance increases sharply when the Sun is near the horizon, disrupting the linear relationship. Each panel shows the linear relationship between TEMPO UV radiance and scattering angle (SA). The analysis demonstrates how the radiance–scattering angle relationship varies with exposure time: (a) 44s on February 6, (b) 12.6s on February 24, (c) 6.3s on March 16, and (d) 3s on April 8, all in 2024. The results highlight the impact of exposure time on radiance behavior, with longer exposures showing stronger positive correlations.

termed as "mirror step" in L1b data), which varies across observations. Typical exposure times for TEMPO include 44, 12.6, 6.3, and 3 s. As illustrated in Figure 1b (and Figure S1 in Supporting Information S1), the scattering angle (γ) is defined as the angle between the direction of incoming sunlight and the direction of the observed radiance (toward the sensor). It is calculated using the following equation:

$$\cos\gamma = -(\cos\theta_s\cos\theta_v + \sin\theta_s\sin\theta_v\cos\varphi)$$

where θ_s is SZA, θ_v is the VZA and φ is the RAZ. Across different exposure times, we observed a relatively stable linear relationship between radiance and scattering angle, with consistent slopes across multiple days (Figure 2). For the scatterplot and corresponding analysis of angles versus radiance, we exclude observations with SZA less than 100° (e.g., close to sunrise and sunset time). When the Sun is too close to the horizon, strong sunlight scattering causes this relationship to break down, leading to a sharp increase in radiance.

The variation of UV radiance with respect to scattering angle in Figure 2 provides insight into the source of background. For example, during twilight observations before sunrise (when the solar zenith angle, SZA, is greater than 90°, i.e., the Sun is below the horizon) in the eastern half of CONUS, the scattering angle increases as the TEMPO scan progresses from east to west (as shown in Figure S2 in Supporting Information S1).

Interestingly, the change in background along the scan direction exhibits opposite trends depending on the exposure time. For longer exposure times, such as 12.6 s, the apparent motion of the Sun (relative to the Earth's surface) is faster than that of the sensor. As the sensor scans westward, it increasingly captures sunlight scattered from the terminator region, leading to a rise in background. This results in a positive correlation between scattering angle and radiance (Figure 2b). In contrast, for shorter exposure times such as 3 s, the sensor scans more rapidly than the Sun's apparent motion. Consequently, as the scan moves westward, less sunlight from the terminator leaks into the field of view, and background decreases. In this case, the relationship between scattering angle and radiance is negative (Figure 2d). This contrast highlights the dynamic interplay among solar geometry, exposure duration, and the relative motion between the sensor and the shifting solar zenith angle across the scan path from east to west. It should be noted that the scattering angle used here does not represent a specific physical scattering event within the scan. Instead, it is used as a geometric parameter describing the relative configuration between the Sun, atmosphere, and sensor. Consequently, the observed relationship between the background signal and scattering angle is empirical rather than derived from a physical scattering model.

TEMPO background comes from a combination of straylight from sunlight and residual errors from dark current correction (Carr et al., 2017, 2025). To mitigate this background and improve data quality, we apply the following correction procedure:

1. Mask out pixels that are invalid, such as those affected by persistently hot or noisy behavior, dark-current over-subtraction, or other non-ideal detector effects. Persistently hot pixels are identified using a 10σ threshold above the nominal level, while anomalously noisy pixels are identified using a 6σ threshold (Carr et al., 2025). Bright urban pixels are classified by applying a 3σ threshold based on Median Absolute Difference (MAD) test (Carr et al., 2025).
2. Granule-based background estimation using scattering angle–based linear correction: for each spectral line across the entire granule, the background is estimated by applying a linear correction based on the relationship between scattering angle (θ) and spectral radiance (as shown in Figure 2). This correction applies a linear fit between scattering angle and radiance to adjust the values accordingly. For each pixel i, the background can be estimated by:

$$B_i(\lambda) = a_\lambda \theta_i + b_\lambda \tag{1}$$

The corrected radiance $L_i'(\lambda)$ after granule-based correction is:

$$L_i'(\lambda) = L_i(\lambda) - B_i(\lambda) \tag{2}$$

This step has two main goals: to reduce radiance values to near-zero for non-city pixels and to remove the systematic linear relationship between scattering angle and radiance within each granule.

3. Scanline-based residual background pattern capture: A 20-scan-line-wide window (W_k), centered on scan line (k) is applied at each spectral wavelength (λ). This window moves across the scan direction, and residual background ($R_k(\theta,\lambda)$) is estimated as the median of the granule-corrected radiances within each window:

$$R_k(\theta,\lambda) = \text{median}_{j\in W_k}(L_j'(\theta,\lambda)) \tag{3}$$

Because twilight-related multi-scattering effects vary by day and viewing geometry, a fixed regression model is not used. Instead, this flexible, data-driven approach adapts to daily variations. In cities with broader east–west extents, masking out city pixels may result in insufficient valid values for estimating background. In such cases, vertical interpolation using surrounding valid pixels is employed to estimate the background.

4. Scanline-based residual background removing: the estimated background pattern from the previous step is used as a reference. For each scan line k, a least-squares method is applied along the scattering-angle dimension to determine the best-fitting slope and intercept that align the granule-corrected radiances with the estimated background pattern.

$$L_k'(\theta,\lambda) = \alpha_k R_k(\theta,\lambda) + \beta_k + \eta_k(\theta) \tag{4}$$

Earth and Space Science 10.1029/2025EA004901

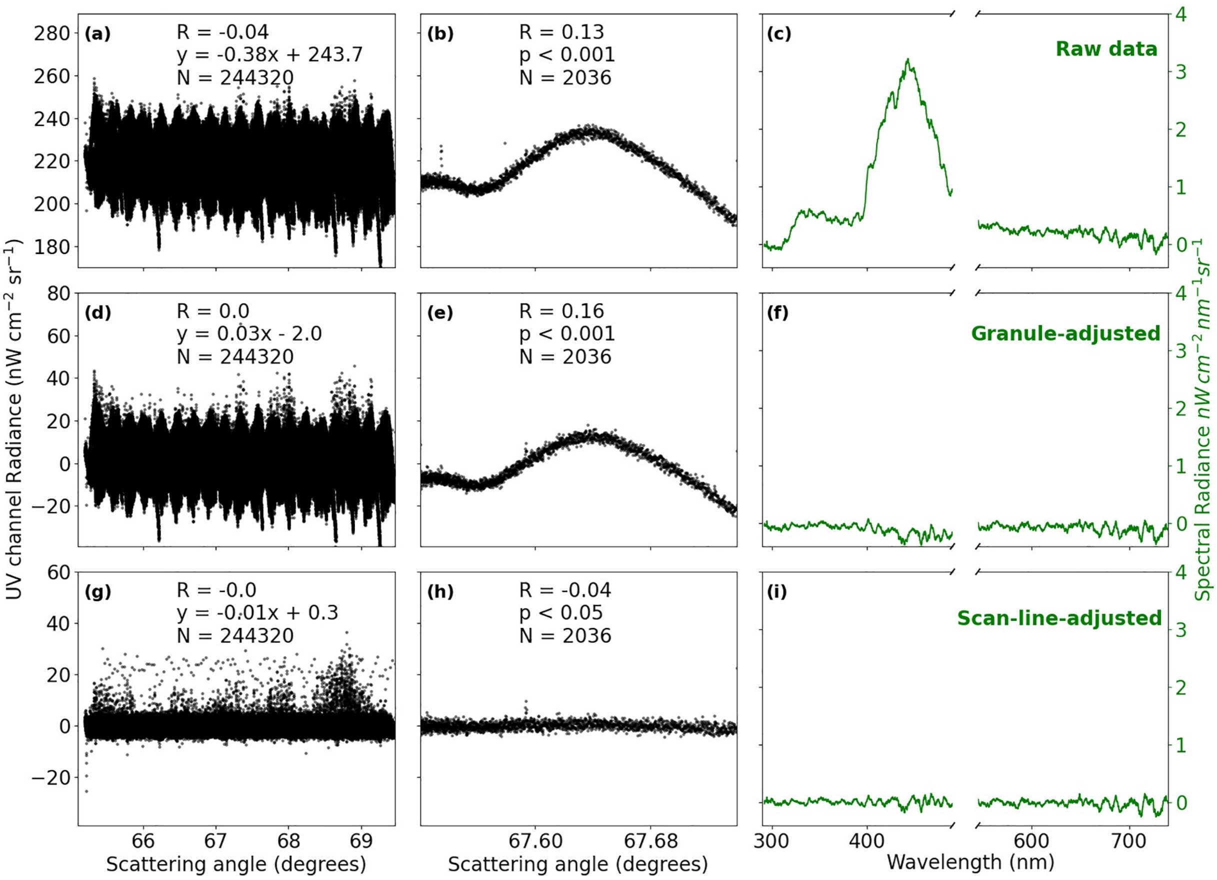

Figure 3. Step-by-step background correction of TEMPO radiance data from March 19th (exposure time: 6 s, TEMPO_RADT_L1_V03_20240319T103217Z_S001G01.nc). The first row shows the raw data without any correction. The second row shows the data after applying correction procedures 2, while the third row shows the data after applying procedure 3 and 4. Please see the text for details. The first column displays the linear correlation between TEMPO UV band radiances (290–490 nm) and scattering angles (SCA) for the entire granule (consisting of 121 scan lines). The second column presents the results for a single scan line. The third column shows the spectral radiance for one pixel. Note, the scales are different between panel (a, d, and g). The first and second column shows the UV band intensity of radiance $(\mathrm{nW\ cm^{-2}sr^{-1}})$ while the third column shows the spectral radiance $(\mathrm{nW\ cm^{-2}nm^{-1}sr^{-1}})$.

The fitted background $\left(\alpha_k R_k(\theta,\lambda) + \beta_k\right)$ is then subtracted from the granule-corrected radiance to obtain the final background-corrected radiance $L_k''(\lambda)$:

$$L_k''(\theta,\lambda) = L_k'(\theta,\lambda) - \left(\alpha_k R_k(\theta,\lambda) + \beta_k\right) \tag{5}$$

City light pixels are also corrected during this step.

5. Mask cloudy pixels using GOES cloud mask data: Cloudy pixels are filtered out by applying the GOES cloud mask product from the closest observation time, reducing cloud contamination in the corrected data.
6. Re-grid TEMPO data to a uniform spatial grid: Since TEMPO's observation geolocations vary daily, all corrected data are re-gridded to a consistent 0.05° spatial resolution over CONUS, ensuring comparability across different days.

The 20-scan-line-wide window size is chosen based on spatial scale and computational efficiency. With TEMPO's ∼4.75 km east–west resolution, a 20-pixel window corresponds to ∼95 km, which exceeds the typical east–west span of most cities in the study region (e.g., Houston is ∼80 km wide). This window size allows representative background regions around cities to be captured while maintaining computational efficiency.

Figure 3 illustrates the contribution of each correction step to background removal for a single granule observed on March 19th (exposure time = 6s). The first row shows the raw data, the second row displays results after correction Step 2, and the third row presents outputs after applying correction Steps 3 and 4. Figure 3a displays the variation in UV radiance (290–490 nm) with scattering angle across the entire granule. As in Figure 2, this relationship is linear, with the slope dependent on exposure time. The granule consists of 121 scan lines oriented in the north–south direction, while the observation moves in the east–west direction. The number of scan lines is not constant and can vary between different scans. Figure 3b shows the variation in UV radiance with scattering angle for a single scan line. Discontinuities may occur at the junction between the upper and lower halves of the scan line due to dark current correction. Figure 3c presents the spectral radiance profile of a single pixel in the northern half of the scan line, where background signal is particularly strong in the UV range (400–490 nm).

Figures 3d–3f show the results after applying the scattering angle–radiance linear correction (Step 2). In Figure 3d, radiance values across the entire granule are reduced to near-zero levels, and the granule-based angular dependence is effectively removed. Since a 6-second exposure time typically exhibits minimal angular dependence (with a slope close to zero), the correction effect is more pronounced for other exposure times (see Figure S3 in Supporting Information S1). Figure 3e shows that, although most background has been eliminated, some scan-line patterns remain visible. Figure 3f demonstrates the successful removal of the pronounced peak in the 400–490 nm range, which is likely caused by straylight effects. Following the subsequent line-by-line corrections (Steps 3 and 4), Figures 3g–3i illustrate the final outcomes. Figure 3g indicates that radiance values within the granule stabilize around a near-zero baseline, though some outliers remain, potentially representing city lights. Although city pixels were initially masked to accurately estimate the background without interference from bright urban areas, the final correction includes all pixels, restoring the city lights in the data set. In Figure 3h, the previously observed curved trend in the scan line radiance has been corrected to yield a flatter profile near zero. This adjustment removes the scanline-based angular dependence of the radiance. Figure 3i demonstrates further refinement of the single-pixel spectral profile, correcting earlier over-adjustments that resulted in negative values within the 400–490 nm range. The final corrected spectrum confirms the successful removal of background twilight residuals, with radiance approaching zero. However, minor positive and negative fluctuations remain due to random noise, which can be effectively minimized by employing multi-day averaging.

Figure 4 presents TEMPO radiance maps over the Houston area, corresponding to the same correction process outlined in Figure 3. Figures 4a–4c show UV radiance (290–490 nm), while Figures 4d–4f display visible radiance (540–640 nm). The first column (Figures 4a and 4d) shows the original data. In the UV channel (Figure 4a), strong background is evident, including over ocean areas where illumination is not expected—radiance values can exceed 240 nW cm^{-2} sr^{-1}. Additionally, a striping pattern aligned with scan lines indicates scan-line-dependent background. In contrast, the visible channel (Figure 4d) is less affected: city lights stand out distinctly from rural surroundings, and background over the ocean is significantly lower than in the UV channel. The second column (Figures 4b and 4e) shows results after applying the scattering angle–radiance linear correction (Step 2). In the UV map (Figure 4b), background is largely reduced to near-zero levels, although vertical striping background persists. A similar effect is seen in the visible map (Figure 4e), where overall background is diminished but some random artifacts remain. After line-by-line correction (Steps 3 and 4), the final column (Figures 4c and 4f) shows that residual vertical striping background is effectively removed. In the UV map (Figure 4c), city shapes become much clearer. In the visible map (Figure 4f), background is also successfully removed, and the city signal appears stronger than in the UV channel, reflecting the fact that most light emissions are concentrated at visible wavelengths.

3.1.2. Spectral Correction Approach

Our second approach for the background correction is based on the intrinsic variation of spectral intensity associated with the solar radiation. While the SCA-based method estimates the background at each wavelength based on the SCA, the second approach, hereafter the spectral approach, remove the background by using the fingerprint or spectral signature of twilight as a whole. The basis for the spectral approach is that the spectral signature (e.g., spectral variation of the intensity) is an inherent propriety of the illumination source, and therefore, the background from solar sources has different spectral signature as compared to that of artificial lights. For example, artificial lights have no emission in the UV wavelengths, while for solar spectra, it not only has UV radiation, but also has the well-defined relationship between the UV radiation and visible radiation.

Figure 5a illustrates the spectral profiles measured by TEMPO over three locations along the same scan line, marked on the inset map by orange, black, and red stars (from north to south). The overlaid gray line represents the solar irradiance spectrum, included for reference. It is clear that at the 300–400 nm, the shape of the scattering

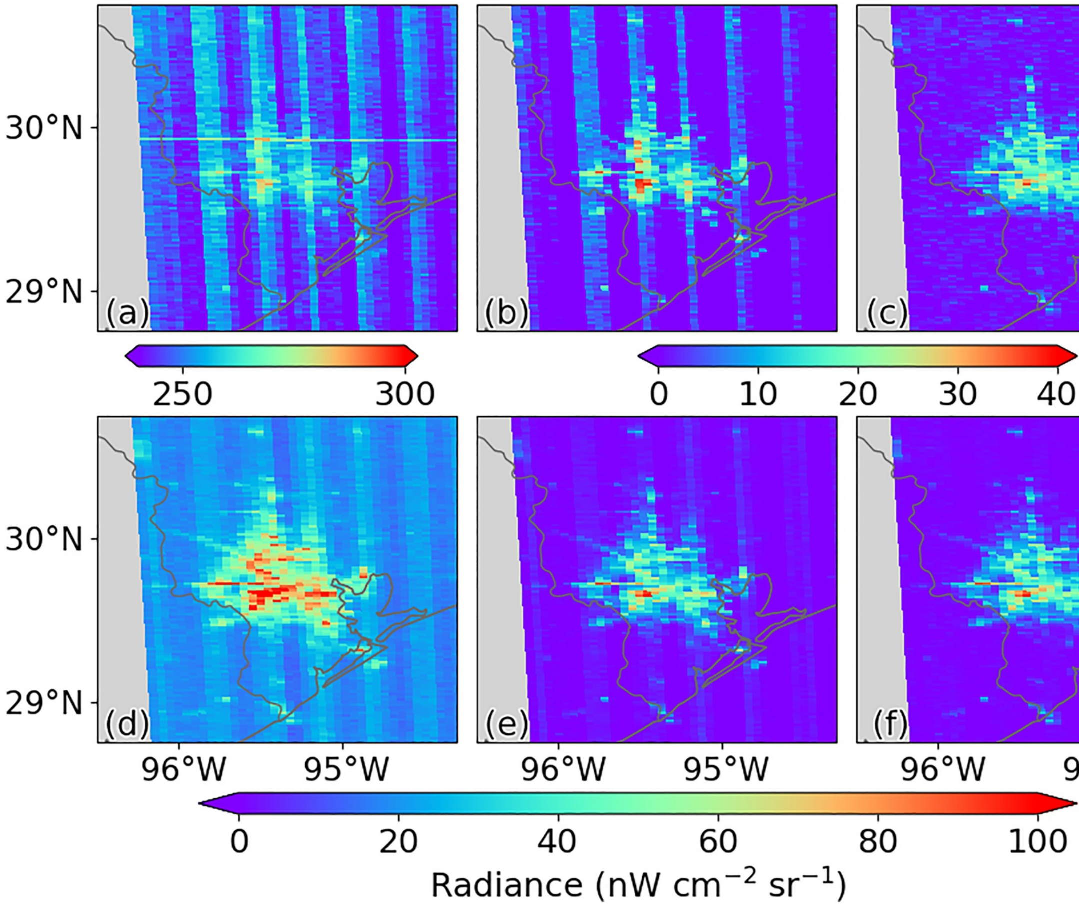

Figure 4. TEMPO band radiance over the Houston area in two spectral ranges: 290–490 nm (first row, (a–c)) and 540–640 nm (second row, (d–f)). The first column (a, d) shows the original data, the second column (b, e) illustrates the data after applying the scattering angle–radiance linear correction (corresponding to Step 2, as shown in the second row of Figure 3), and the third column (c, f) displays the results following the line-by-line corrections (Steps 3 and 4, corresponding to the third row of Figure 3).

spectra measured by TEMPO remain very similar to that of spectra of solar radiation (before reaching the atmosphere). The shape difference between the two can originate from atmospheric scattering, absorption, and geometry. For example, twilight spectra are generally blue-shifted relative to the solar spectrum (Figure 5a); this can be explained by the strong Rayleigh scattering at blue wavelength. Indeed, along the scan line (2048 pixels ~ 6144 km), the shape of the twilight spectrum remains relatively consistent over each pixel regardless the

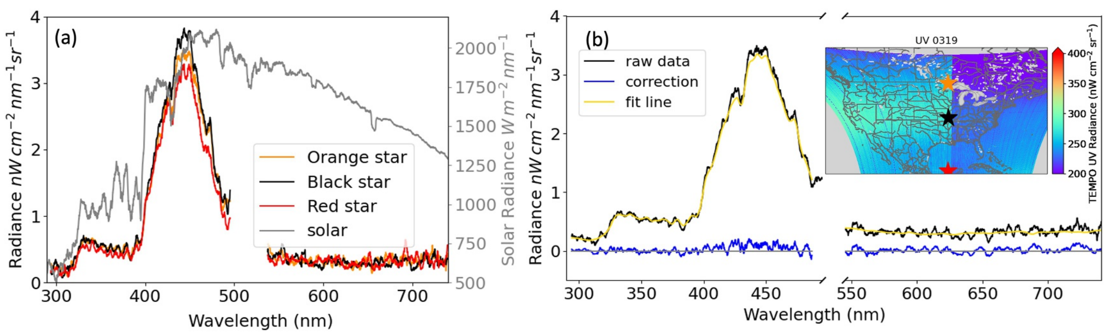

Figure 5. (a) Spectral profiles of three locations along the same TEMPO scan line, marked by orange, black, and red stars (from north to south) on the inset map in panel (b). The gray line represents the solar irradiance spectrum for reference. (b) Spectral profile at the black star location, showing the raw data (black line), the fitted line using the estimated twilight spectrum (yellow line), and the corrected spectrum (blue line).

observation location (over the ocean or over the land; Figure 5b). The inset map in Figure 5b marks the three locations, all along a single scan line.

To consider the slight variation of profile (shape and intensity) of twilights along the scan line, a moving window with a width of 20 pixels along the vertical scan line is used. The window must remain sufficiently localized to avoid excessive spatial variation in twilight stray light. A 20-pixel window provides a practical balance between capturing representative background statistics and limiting the impact of large-scale background gradients. Subsequently, the spectral-based correction is applied on the basis of each scan line as follows:

1. Window selection: The pixel type (city or non-city) is first identified using a 3σ threshold based on the MAD (Carr et al., 2025). Subsequently, for each target pixel, a window consisting of the 20 surrounding pixels is selected if more than 85% are valid and classified as non-city. 85% is chosen to allow some tolerance for potential classification errors or mixed pixels within the window. If this condition is not met, the window is shifted upward or downward to locate the nearest window that satisfies this criterion.
2. For each pixel i with its associated window Ω_i:

We evaluated the sensitivity of the background estimation to different statistical estimators and found that the optimal choice depends on pixel type (details described in—Text S3 in Supporting Information S1).

- If i is a city pixel, estimate the background spectrum as the median across Ω_i:

$$T_i(\lambda) = \text{median}\{\mathrm{S_j}(\lambda) | j \in \Omega_i\} \tag{6}$$

Where $S_j(\lambda)$ represents the measured spectrum at pixel j over wavelength λ, and $j \in \Omega_\mathrm{i}$ indicates pixels within the window surrounding the target pixel i. The resulting median spectrum serves as the estimated twilight background spectrum for pixel i.

- If i is a non-city pixel, estimate the background spectrum as the 80th percentile across Ω:

$$T_i(\lambda) = \text{quantile}_{0.8}\{S_j(\lambda) | j \in \Omega_i\} \tag{7}$$

3. Linear Regression for Background Modeling:

For each individual pixel:

- Extract the spectral profile at 290–390 nm ($S_i^{\mathrm{UV}} = S_i(\lambda), \lambda \in [290, 390]$ nm), a spectral region where contributions from city lights are minimal and the signal is dominated by twilight.
- Perform a linear regression between the extracted spectrum (S_i^{UV}) and the estimated twilight spectrum within this range ($T_i^{\mathrm{UV}} = T_i(\lambda), \lambda \in [290, 390]$ nm):

$$S_i^{\mathrm{UV}} = a_i \cdot T_i^{\mathrm{UV}} + b_i \tag{8}$$

- Use the fitted regression model to predict the background signal across the remaining spectral ranges: 390–490 nm and 540–740 nm:

$$B_i(\lambda) = a_i \cdot T_i(\lambda) + b_i, \qquad \lambda \in \{[390, 490] \cup [540, 740]\ \text{nm}\} \tag{9}$$

4. Background Subtraction: Subtract the estimated background spectrum from the original pixel spectrum to generate the corrected pixel spectral profile:

$$S_i^{\mathrm{c}}(\lambda) = S_i(\lambda) - B_i(\lambda) \tag{10}$$

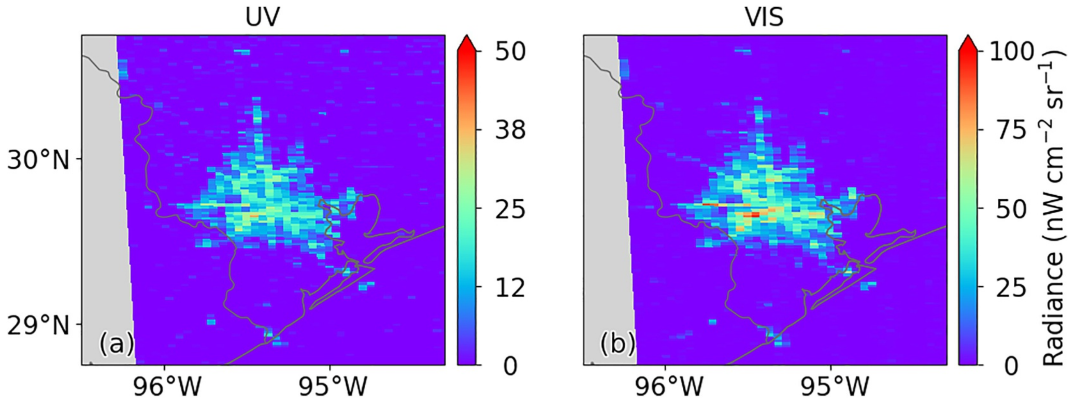

Figure 6. Spectrum–corrected radiance map over the Houston area on 19 March 2024, corresponding to the same granule shown in Figures 3 and 4. (a) UV channel (290–490 nm); (b) Visible (VIS) channel (540–640 nm).

Figure 5b presents spectral data at the location marked by a black star in the inset map, including the raw radiance spectrum (blue line), the estimated twilight spectrum (red line), and the corrected spectrum (green line). Since this location is over the ocean and near the coastline, artificial lighting signals are weak, resulting in a corrected spectrum that is nearly zero across all wavelengths. The estimated twilight spectrum closely matches the raw data within the fitting range (290–390 nm) but is slightly lower near 450 nm, where twilight radiance peaks. Two factors may contribute to this discrepancy: inherent uncertainties and fluctuations in the estimated twilight spectrum, or the presence of faint blue light emissions from ships or other minor sources. This methodology leverages the assumption that artificial lights have negligible signals within the 290–390 nm range, attributing any significant excess radiance beyond the estimated twilight spectrum to artificial lighting.

Figure 6 presents the corrected radiance maps over the Houston region on 19 March 2024, for the UV channel (Figure 6a) and the VIS channel (Figure 6b). As expected, the VIS channel map remains clear, while the UV map shows reduced background compared to Figure 4c. The improvement becomes more apparent when the value range is adjusted (see Figure S8 in Supporting Information S1). The window size used for estimating twilight spectra is critical for this method. Within this narrow window, background is assumed to be slowly varying. Because moonlight is linked to surface reflectance, we assume surface properties remain stable over such a small area. As a result, both moonlight and twilight contributions can be incorporated into the background. With the appropriate window size, this spectral correction effectively removes both twilight and moonlight, producing more stable results for the UV band.

It is important to note that both maps are generated by integrating radiance over a range of bandwidths—for example, the UV map represents integrated radiance from 290 to 490 nm. Sensor performance can vary across different days depending on exposure time. If too many spectral wavelengths are flagged as anomalously noisy pixels, the resulting integrated radiance will be much lower (Figure S7 and Text S4 in Supporting Information S1). This effect is more pronounced in the UV channel, since background tends to be concentrated in this spectral range.

3.1.3. Combination of Two Correction Approaches as SLAN Algorithm

The differences become more evident when comparing the spectra before and after applying the two correction methods, as shown in Figure 7. In this comparison, we examine two example pixels: one located over the ocean (Figure 7a) and the other within the city region (Figure 7b).

For the ocean pixel (Figure 7a), both the VIS and UV channels should approach zero after correction, as no artificial lights are present at night. The VIS radiances are similar for both correction methods. However, in the UV, particularly at blue wavelengths (400–490 nm), the spectral approach-corrected spectra show lower values compared to those corrected using the scattering-angle method. This reflects the higher UV background in the scattering-angle correction and indicates that the spectral approach performs better at reducing blue-channel background in this case. For the city pixel (Figure 7b), both methods generally perform similarly across most city-light pixels, showing nearly identical spectral profiles and radiance intensities. Minor differences occur

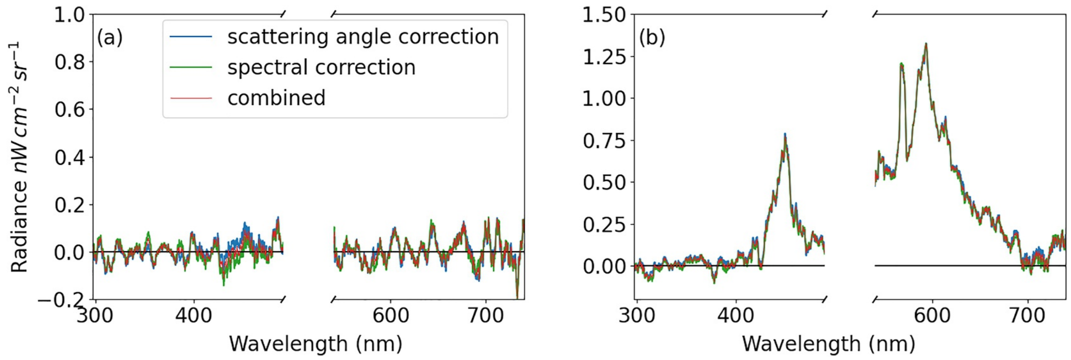

Figure 7. Comparison of corrected spectral profiles using scattering angle correction and spectral correction, and their combined results over (a) the ocean and (b) city-light pixels.

primarily at shorter wavelengths, but the overall agreement indicates that both approaches effectively correct the radiance signal.

To leverage the strengths of each method and having a more stable solution across a wide rage of observing conditions (Text S5 in Supporting Information S1), we average the two corrections in both channels to obtain the final correction. This method improves overall accuracy and more effectively suppresses background in the blue band.

3.2. Georeferenced Uncertainties and Correction

Figure 8 displays city light maps over the Houston area for selected clear days, with freeway locations overlaid for geographic reference. A red circle highlights a major north–south freeway in northern Houston, which serves as a convenient geolocation reference. The maps shown here use the original TEMPO spatial grids and have not yet been re-gridded. Ideally, the city light patterns should align with the freeway. However, across the three selected days, the observed city lights shift approximately three pixels from east to west. This positional instability may introduce challenges in subsequent processing steps, such as multi-day averaging and pixel-level comparisons with Black Marble products. Therefore, a geolocation correction is applied following the method described in the (Text S7 in Supporting Information S1).

4. Evaluation and Discussion

This section evaluates TEMPO observations against two established references (Black Marble and ISS nighttime photography) over the Houston metropolitan area. Houston was selected as a test site because of its extensive artificial light emissions, which generate strong, widespread signals that provide a robust basis for assessing

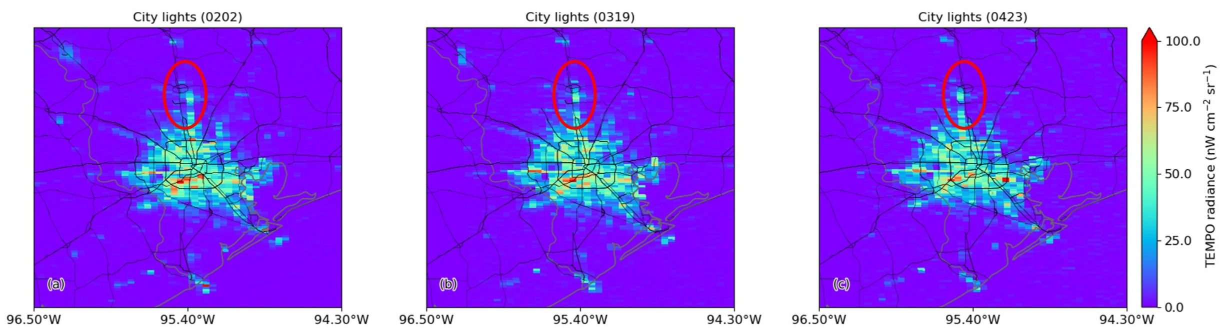

Figure 8. TEMPO city light maps over Houston after background correction for selected days. (a) Feb 2nd (b) March 19th (c) April 23rd. The freeways and roads are overlaid as a spatial reference, highlighting the noticeable shifts in geometry across different days. These spatial variations suggest potential instability or inconsistencies in the georeferencing of the TEMPO data set over time.

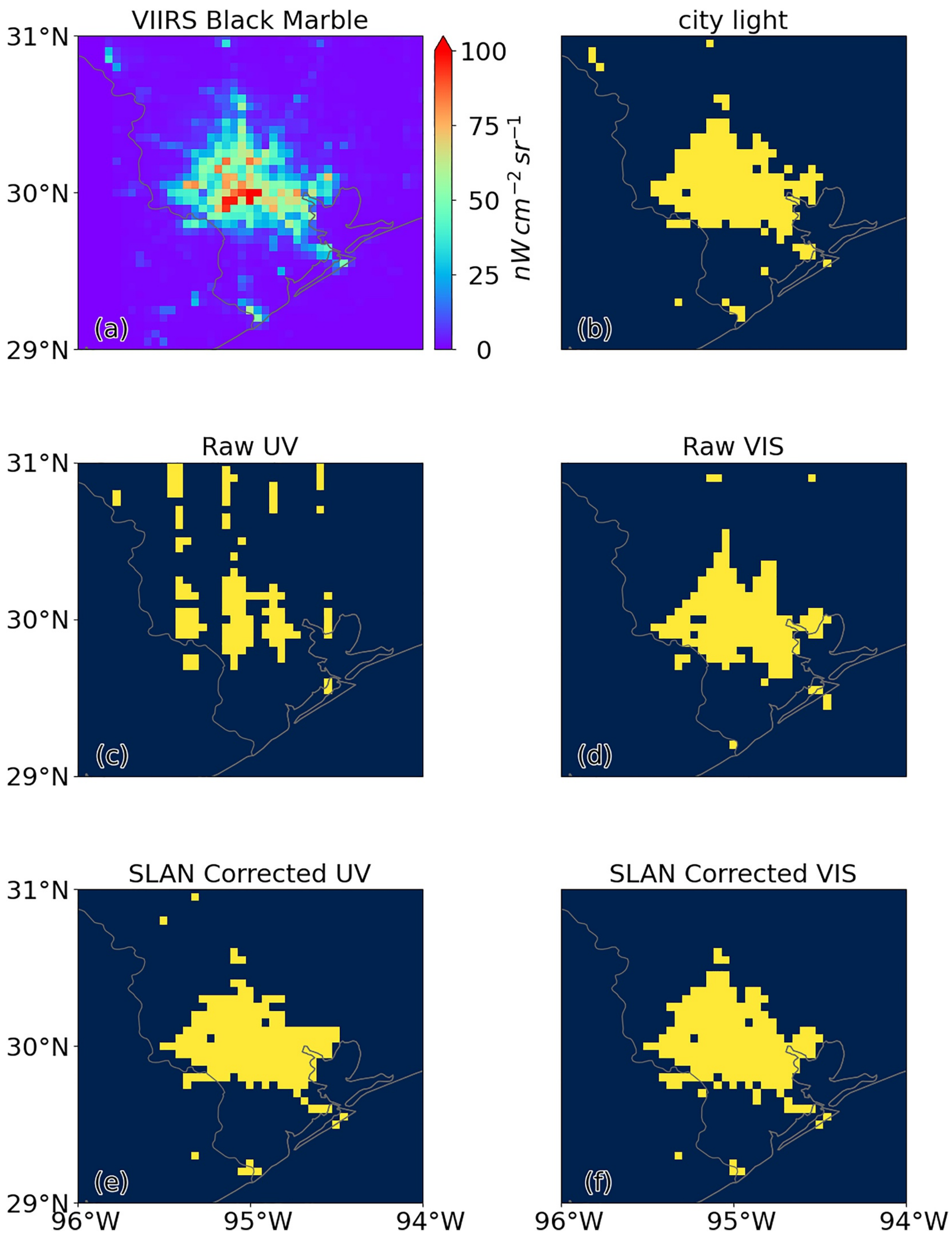

Figure 9. (a) Nighttime radiance from NASA's Black Marble on 19 March 2024. (b) City-light mask derived from (a) via thresholding (yellow indicate city pixels) (c, d) City-light masks from *raw* TEMPO data on 19 March 2024 based on UV (290–490 nm) and VIS (540–740 nm) spectra, respectively (e, f) City-light masks from corrected TEMPO data for the same date based on UV (290–490 nm) and VIS (540–740 nm) spectra, respectively.

TEMPO's performance. The city was also chosen because of the availability of high-quality ISS images collected over this region in recent years. Given the relatively coarse spatial resolution of the newly released TEMPO twilight data set, the higher-resolution Black Marble and ISS imagery serve as reliable benchmarks for validation.

Table 1
Confusion Matrix Showing the Performance of City Light Detection From Raw TEMPO Data and Different Correction Approaches

Raw UV	True positive (%)	True negative (%)	Raw VIS	True positive (%)	True negative (%)
Predicted positive (%)	30.6	3.4	Predicted positive (%)	61.9	1.6
Predicted negative (%)	69.4	96.6	Predicted negative (%)	38	98.4
SLAN corrected UV	**True positive (%)**	**True negative (%)**	**SLAN corrected VIS**	**True positive (%)**	**True negative (%)**
Predicted positive (%)	96.3	5.6	Predicted positive (%)	94.3	4.6
Predicted negative (%)	3.7	94.4	Predicted negative (%)	5.7	95.4

4.1. Assessment of City Light Detection and Brightness in SLAN Data

Figure 9a shows the Black Marble radiance map resampled to 0.05° over Houston on 19 March 2024, while Figure 9b presents the corresponding city light classification using a 10 nW cm^{-2} sr^{-1} threshold. Figures 9c and 9d display UV- and VIS-band radiance from raw TEMPO data over the same region. The UV band exhibits clear scanline background, whereas the VIS band more closely aligns with the Black Marble city outlines. Using the Black Marble classification as ground truth, raw TEMPO data in the UV band correctly identifies only 30.6% of city lights, compared with 61.9% in the VIS band, highlighting the UV band's higher sensitivity to background. Although differences in wavelength coverage, spectral response, and observation time between the sensors affect absolute radiance values, city light classifications remain broadly comparable.

Correction procedures or SLAN algorithm were applied to mitigate background using a combination of scattering-angle and spectral corrections. To address day-to-day geolocation shifts, TEMPO data were further aligned to the Black Marble reference through pixel-level adjustments. Figures 9e and 9f shows the resulting improvements: the corrected UV band delineates city boundaries with accuracy comparable to both the VIS band and the Black Marble map. Following these corrections, overall city light detection accuracies for both bands increased to more than 90% (Table 1), representing gains of 65% for the UV band and 32% for the VIS band.

Consistency with DNB is further quantified in Figure 10, which compares DNB radiance with TEMPO VIS-band radiance (540–740 nm) under three conditions. In the raw case (Figure 10a), the relationship is moderately strong ($R = 0.65$) but exhibits a positive intercept of ~37 ($nWcm^{-2}sr^{-1}$), indicating a bias consistent with background and overestimation at low signal. After background correction (Figure 10b), the correlation improves slightly ($R = 0.79$) while the RMSE drops sharply from ~42.1 to 8.6, showing that the correction effectively removes much of the background offset and compresses residual spread about the 1:1 line. A subsequent geolocation shift (Figure 10c) further improves the comparison, raising the correlation to 0.9 and lowering RMSE further to 6.4 (≈85% reduction from raw), consistent with reduced spatial mismatches between sensors. Together, these results suggest that the dominant error in the raw TEMPO radiance is background signals and that spatial misregistration

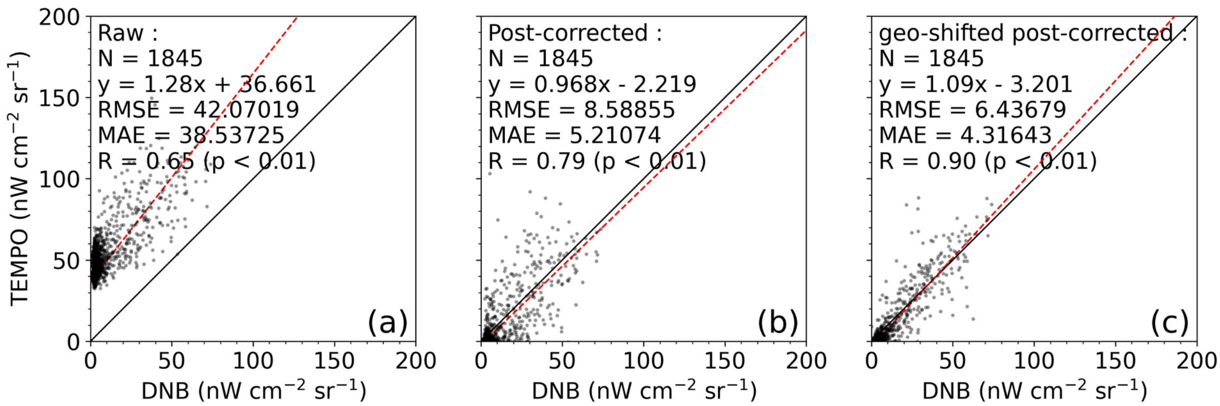

Figure 10. Scatterplot comparisons of Black Marble (DNB) radiance with TEMPO VIS-band radiance (540–740 nm). (a) DNB versus raw TEMPO radiance, (b) DNB versus post-correction TEMPO radiance by spectral light at night algorithm, and (c) DNB versus geolocation-shifted post-correction TEMPO radiance. The corrections progressively improve agreement with the Black Marble reference.

Earth and Space Science
10.1029/2025EA004901

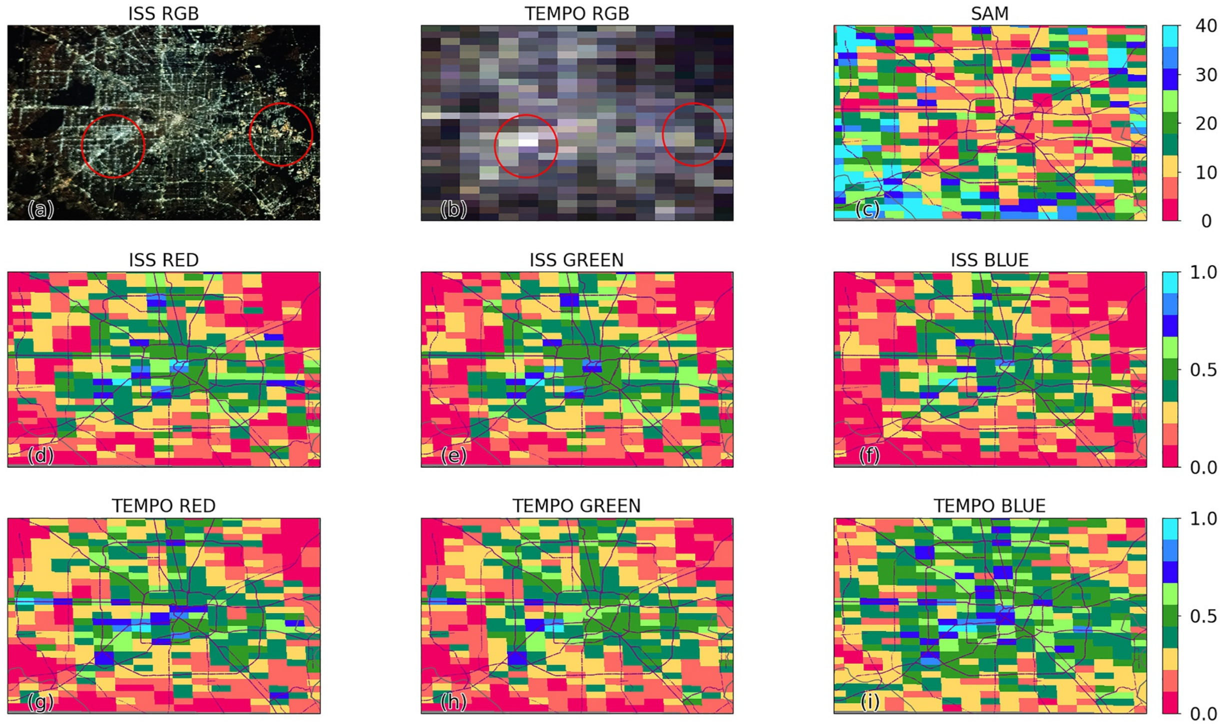

Figure 11. (a) RGB image from International Space Station (ISS) photography acquired on 17 January 2024; (b) RGB image from TEMPO nighttime observations on 19 March 2024; (c) Spectral Angle Mapper (SAM) values computed among normalized red, green, and blue channels from the ISS and TEMPO data. Higher SAM values indicate lower spectral similarity, while lower values indicate greater spectral similarity (d–i) Normalized red, green, and blue channel values for ISS photography and TEMPO data: (d) ISS red, (e) ISS green, (f) ISS blue, (g) TEMPO red, (h) TEMPO green, (i) TEMPO blue.

contributes appreciably to the remaining variance; addressing both brings TEMPO into close agreement with DNB for these scenes.

4.2. Assessment of Spectral Brightness in SLAN Data

The ISS RGB night photograph on 17 January 2024 (Figure 11a) captures Houston's urban lighting pattern with strong spatial structure and clear color variation. Brightness peaks at the city center and along the southwestern side (red circled area), where dense, high-intensity white lighting outlines a compact urban core and major roadways. On the east side (red-circled), large contiguous blocks emit yellow lights, suggesting extensive facilities or districts illuminated by similar warm-toned lamps. In contrast, the southwest circled region displays chains of white to bluish lights aligned with major roads. These whiter, cooler tones and linear geometries are indicative of newer, higher–color-temperature sources (e.g., LEDs) concentrated along key transportation corridors. Toward the city edges, brightness gradually declines, giving way to patchy dark zones likely corresponding to water bodies or parks.

The corresponding TEMPO nighttime observations from 19 March 2024 (Figure 11b) reveal similar large-scale patterns as that from ISS night photograph but at a much coarser spatial resolution. A larger spatial coverage view from TEMPO is shown in Figure S11 in Supporting Information S1 to better illustrate the city outlines. The eastern circled area remains predominantly yellow, while the southwest retains its white/blue signature. The RGB vectors for the ISS and TEMPO data were obtained following the method described in the (Text S8 in Supporting Information S1).

To enable pixel-wise comparison, we resampled the ISS image to the TEMPO grid and normalized both data sets to (0, 1) per channel (Figures 11d–11i). Because Nikon digital counts are not directly comparable to TEMPO radiances, normalization supports relative rather than absolute comparisons. Broad spatial patterns are consistent across sensors: low values dominate the periphery, while high values cluster along the urban core and major roads. The ISS panels exhibit sharper contrasts and finer spatial heterogeneity, whereas TEMPO shows blockier textures and smoother gradients, reflecting its coarser footprint. Channel by channel, the green and red band show strong correspondence ($R_{\text{green}} = 0.82$, $R_{\text{red}} = 0.82$) with co-located mid/high values along central roads and downtown; blue shows the weakest agreement ($R_{\text{blue}} = 0.73$). All three correlations are statistically significant ($p < 0.0001$), indicating a strong agreement between data sets. The lower blue correlation likely reflects the temporal mismatch (January vs. March) and the intervening shift toward LED lighting, which increases blue–green emission relative to red. Additional contributors may include seasonal lighting (e.g., Christmas lighting and Lunar New Year displays), differences in sensor spectral response, viewing geometry, and atmospheric conditions. Overall, TEMPO recovers the main spatial structure seen by the ISS but with coarser spatial detail and band-dependent fidelity—most notably in the blue channel.

Figure 11c maps the Spectral Angle Mapper (SAM, θ) between ISS RGB vectors ($y = [y_R, y_G, y_B]$) and TEMPO RGB vectors ($x = [x_R, x_G, x_B]$), computed after normalization to the TEMPO grid:

$$\theta = \cos^{-1}\left(\frac{x \cdot y}{||x|| \cdot ||y||}\right)$$

Because SAM measures the angle between two spectra, lower values indicate greater spectral similarity and higher values indicate larger spectral differences. SAM minima cluster in downtown Houston and along major transportation corridors, indicating that the relative RGB composition in these bright areas is closely matched between sensors. SAM values rise toward the city's edges. The region-wide mean SAM is 16°, but restricting to pixels with normalized TEMPO red-channel radiance >0.5 yields a mean of 6.7°. Together, these patterns show that TEMPO reproduces the ISS spectral "signature" most closely in the bright urban core and along major corridors, while discrepancies grow where lighting is heterogeneous, dim, or has changed in composition (e.g., LED adoption or seasonal lighting) between January and March 2024.

4.3. Nighttime Light Map Comparison Over CONUS

Figure 12 compares nighttime light distributions across the contiguous United States (CONUS) using: VIIRS DNB, TEMPO VIS, and TEMPO UV. The VIIRS DNB (500–900 nm) Black Marble map (Figure 12a) reveals a high level of spatial detail, capturing both bright urban centers and faint emissions extending into surrounding suburban and rural areas. The TEMPO VIS band (540–740 nm) map (Figure 12b) displays a coarser spatial pattern with blockier structures and reduced sensitivity to low-radiance features. Although the major cities remain prominent, the surrounding dimmer regions are less well defined, likely due to differences in spatial resolution, spectral coverage and instrument sensitivity between VIIRS and TEMPO. The TEMPO UV band (290–490 nm) map (Figure 12c) displays a much weaker and cleaner signal than the VIS channel, with visible emissions largely confined to the largest urban centers. Notably, the bright regions observed in the VIS map over the Permian Basin and North Dakota largely disappear in the UV band, consistent with the spectral characteristics of gas flaring emissions: stronger at visible wavelengths and much weaker in the UV. Additionally, point-like signals aligned with major highways, such as Interstate 70, are discernible in the central U.S., indicating the influence of transportation lighting on the nocturnal radiance patterns. Overall, this comparison highlights the complementary capabilities of VIIRS and TEMPO instruments for monitoring nighttime light, revealing how spectral and spatial resolution differences shape the observed radiance patterns across CONUS.

5. Summary and Conclusions

In this study, we developed two background removal methods for TEMPO twilight data sets to generate spectral-resolved light at night (SLAN): a scattering-angle correction and a spectral correction. In the first method, we use the relationship between scattering angle and radiance to remove background at both the granule and scanline levels (two steps). This approach effectively suppressed background in both the UV and visible bands, though some residual signal remained, potentially from scattered moonlight. To address this, we introduced a second method, the spectral correction. Because most artificial light sources are designed to minimize UV emissions, spectra below 390 nm can be used to estimate direct twilight contributions, enabling isolation and quantification of city-light signals. Operationally, we estimate the background within a narrow spatial window so that background terms vary slowly across the window; since moonlight is tied to surface reflectance, it is also measured as part of the twilight, provided surface properties are stable within this small area. Combining the two methods formulate the SLAN algorithm to yield more stable corrections. We also observed a geolocation mismatch

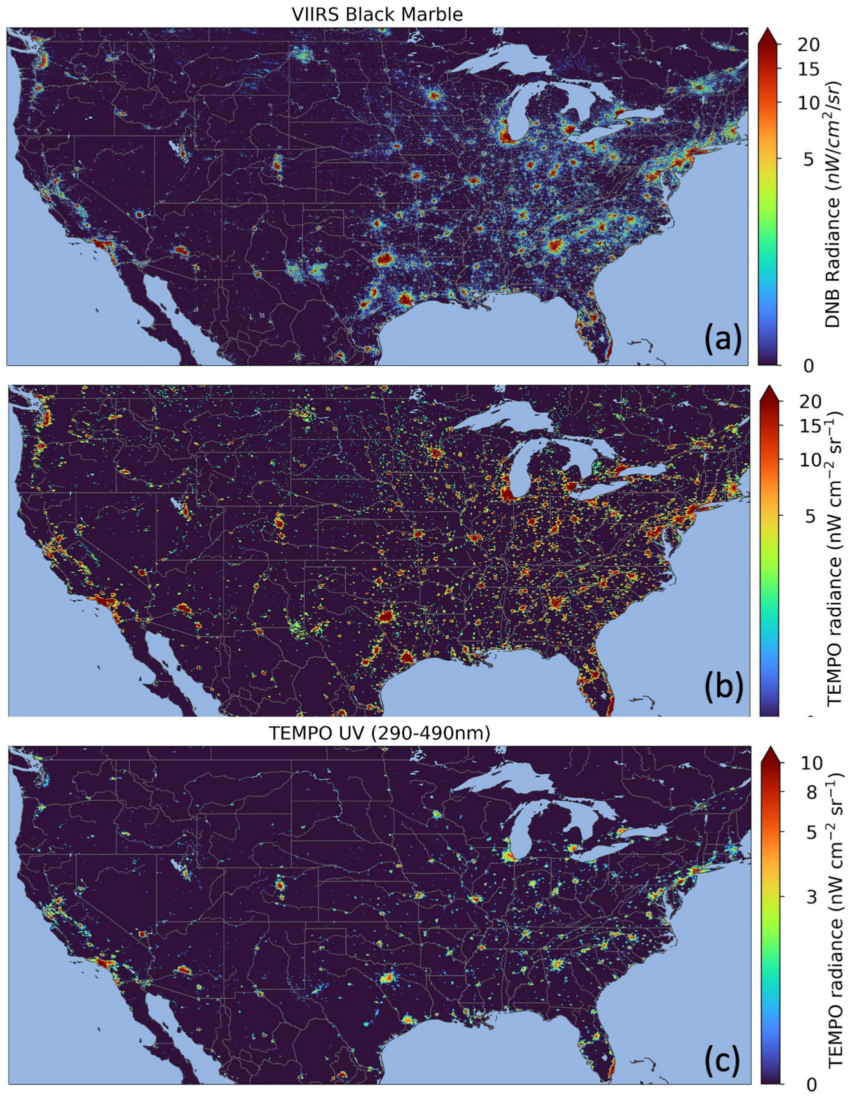

Figure 12. Nighttime light maps over the CONUS region derived from (a) the VIIRS Black Marble product, (b) the TEMPO visible (VIS) band (540–740 nm), and (c) the TEMPO ultraviolet (UV) band (290–490 nm).

between different days in the current version of the data, which may be improved or corrected in future releases by collocating with VIIRS DNB observations.

We then evaluated the SLAN data product from TEMPO observations against two established references: VIIRS Black Marble and ISS nighttime photography over the Houston metropolitan area. The results show that post-corrected TEMPO data by the SLAN algorithm reliably reproduce urban light patterns despite differences in spectral characteristics and observation timing relative to Black Marble. Comparisons with ISS imagery show that TEMPO most closely matches the ISS spectral “signature” in bright urban cores and along major roads, with differences increasing in dimly lit areas or where lighting composition changed between January and March 2024. Finally, we compared nighttime light maps over the CONUS region using three bands: VIIRS DNB, TEMPO VIS, and TEMPO UV. The TEMPO VIS band aligns more closely with VIIRS DNB, while in regions with gas flaring emissions, both VIIRS DNB and TEMPO VIS differ markedly from the TEMPO UV band. These contrasts illustrate how VIIRS and TEMPO together enhance our ability to characterize and monitor diverse nighttime lighting sources.

Overall, this study advances the use of TEMPO twilight observations for ALAN research by introducing algorithmic approaches specifically designed to stabilize background removal and enable retrieval of spectrally resolved nighttime lighting signals. In contrast to previous work that primarily focused on demonstrating nighttime light detection capability in visible wavelengths, the SLAN framework developed here allows consistent separation of background contributions and enables the use of short-wavelength (including UV) information for light-source characterization and ecological exposure studies. These developments complement existing TEMPO nighttime analyses and highlight the potential of combining TEMPO spectral observations with broadband sensors such as VIIRS DNB to improve monitoring of artificial lighting and its environmental impacts.

A key long-term objective of the TEMPO SLAN product is to enable research into the differential environmental and biological impacts of artificial light sources, particularly their spectral characteristics. By providing spectrally resolved nighttime observations, TEMPO offers new opportunities to investigate how wavelength composition influences ecological systems, human and animal biology, and the evolution of lighting technologies. These observations can also help track regional and temporal changes in light-source composition associated with urban development and other anthropogenic activities. Ultimately, this capability supports efforts to balance the societal benefits of nighttime illumination with the need to reduce ecological disruption from artificial light at night (ALAN).

Conflict of Interest

The authors declare no conflicts of interest relevant to this study.

Availability Statement

TEMPO data are available at NASA/LARC/SD/ASDC (2024). VIIRS Black Marble data are available at Román et al. (2018a, 2028b). ISS imagery is available at NASA Johnson NASA Johnson Space Center (2024). GOES cloud mask data are available at GOES-R Algorithm Working Group and GOES-R Series Program (2018). The background-corrected data sets for the March 19 case study are available at Xue (2026).

Acknowledgments
We would like to thank the entire TEMPO team for providing the twilight data set. TEMPO twilight data were obtained from the NASA Langley Research Center Atmospheric Science Data Center. We also acknowledge the Earth Science and Remote Sensing Unit at NASA Johnson Space Center for the ISS photography information, NASA LAADS DAAC for the Black Marble product, and the NOAA National Centers for Environmental Information (NCEI) for the level-2 GOES cloud mask products. This work is supported by TEMPO Grant (with subcontract number SV7-87011) from Smithsonian to the University of Iowa, NASA's TEMPO/GEO-XO program (Grant. 80NSSC25K0221) and NASA's Health and Air Quality Applied Science Team (HAQST) program (Grant. 80NSSC21K0510). X.L. would like to thank NASA for funding the TEMPO mission and its operation through contracts NNL13AA09C and 80MSFC24CA004.

References

Bennie, J., Davies, T. W., Cruse, D., & Gaston, K. J. (2016). Ecological effects of artificial light at night on wild plants. *Journal of Ecology*, *104*(3), 611–620. https://doi.org/10.1111/1365-2745.12551

Bolton, D., Mayer-Pinto, M., Clark, G., Dafforn, K., Brassil, W., Becker, A., & Johnston, E. (2017). Coastal urban lighting has ecological consequences for multiple trophic levels under the sea. *Science of the Total Environment*, *576*, 1–9. https://doi.org/10.1016/j.scitotenv.2016.10.037

Carr, J., Liu, X., Baker, B., & Chance, K. (2017). Observing nightlights from space with TEMPO. *International Journal of Sustainable Lighting*, *19*(1), 26–35. https://doi.org/10.26607/ijsl.v19i1.64

Carr, J. L., Chong, H., Liu, X., Houck, J. C., Kalb, V., Madani, H., et al. (2025). TEMPO at night. *Earth and Space Science*, *12*(10), e2024EA004157. https://doi.org/10.1029/2024ea004157

Chong, H., Liu, X., Houck, J., Flittner, D. E., Carr, J., Hou, W., et al. (2026). Algorithm theoretical basis for version 3 TEMPO level 0–1 processor. *Earth and Space Science*, *13*(2), e2025EA004516. https://doi.org/10.1029/2025ea004516

Cinzano, P., Falchi, F., & Elvidge, C. D. (2001). The first world atlas of the artificial night sky brightness. *Monthly Notices of the Royal Astronomical Society*, *328*(3), 689–707. https://doi.org/10.1046/j.1365-8711.2001.04882.x

Davies, T. W., Bennie, J., Inger, R., De Ibarra, N. H., & Gaston, K. J. (2013). Artificial light pollution: Are shifting spectral signatures changing the balance of species interactions? *Global Change Biology*, *19*(5), 1417–1423. https://doi.org/10.1111/gcb.12166

Davies, T. W., Coleman, M., Griffith, K. M., & Jenkins, S. R. (2015). Night-time lighting alters the composition of marine epifaunal communities. *Biology Letters*, *11*(4), 20150080. https://doi.org/10.1098/rsbl.2015.0080

Davies, T. W., & Smyth, T. (2018). Why artificial light at night should be a focus for global change research in the 21st century. *Global Change Biology*, *24*(3), 872–882. https://doi.org/10.1111/gcb.13927

Dominoni, D., Quetting, M., & Partecke, J. (2013). Artificial light at night advances avian reproductive physiology. *Proceedings of the Royal Society B: Biological Sciences*, *280*(1756), 20123017. https://doi.org/10.1098/rspb.2012.3017

Falchi, F., Cinzano, P., Duriscoe, D., Kyba, C. C., Elvidge, C. D., Baugh, K., et al. (2016). The new world atlas of artificial night sky brightness. *Science Advances*, *2*(6), e1600377. https://doi.org/10.1126/sciadv.1600377

Frank, K. D. (1988). Impact of outdoor lighting on moths: An assessment.

Gaston, K. J., Davies, T. W., Nedelec, S. L., & Holt, L. A. (2017). Impacts of artificial light at night on biological timings. *Annual Review of Ecology, Evolution, and Systematics*, *48*(1), 49–68. https://doi.org/10.1146/annurev-ecolsys-110316-022745

Gaston, K. J., & Sánchez de Miguel, A. (2022). Environmental impacts of artificial light at night. *Annual Review of Environment and Resources*, *47*(1), 373–398. https://doi.org/10.1146/annurev-environ-112420-014438

GOES-R Algorithm Working Group and GOES-R Series Program. (2018). NOAA GOES-R sSeries Advanced Baseline Imager lABI) Level c slear mky Mask [Dataset]. *NOAA National Centers for Environmental Information*. https://doi.org/10.7289/V5SF2TGP

Heidinger, A. (2011). *Algorithm theoretical basis document: ABI cloud mask*. University of Wisconsin.

Johnson, B. (2020). Detecting impervious cover with artificial lighting in astronaut photography from the international space station.

Kelber, A., Yovanovich, C., & Olsson, P. (2017). Thresholds and noise limitations of colour vision in dim light. *Philosophical Transactions of the Royal Society B: Biological Sciences*, *372*(1717), 20160065. https://doi.org/10.1098/rstb.2016.0065

Knop, E., Zoller, L., Ryser, R., Gerpe, C., Hörler, M., & Fontaine, C. (2017). Artificial light at night as a new threat to pollination. *Nature*, *548*(7666), 206–209. https://doi.org/10.1038/nature23288

Liao, L., Weiss, S., Mills, S., & Hauss, B. (2013). Suomi NPP VIIRS day-night band on-orbit performance. *Journal of Geophysical Research: Atmospheres*, *118*(22), 12705–712718. https://doi.org/10.1002/2013jd020475

Middlemiss, K. L., Cieraad, E., Mander, S., Fischer, J. H., & Goad, D. (2025). Understanding the impacts of LED light pollution in marine ecosystems: Phototaxis response in fairy prion. *Journal of Ornithology*, *166*(3), 1–13. https://doi.org/10.1007/s10336-024-02245-1

Mills, S., Weiss, S., & Liang, C. (2013). VIIRS day/night band (DNB) stray light characterization and correction. In *Paper presented at the Earth observing systems XVIII*.

Naeger, A. R., Newchurch, M. J., Moore, T., Chance, K., Liu, X., Alexander, S., et al. (2021). Revolutionary air-pollution applications from future tropospheric emissions: Monitoring of pollution (TEMPO) observations. *Bulletin of the American Meteorological Society*, *102*(9), E1735–E1741. https://doi.org/10.1175/bams-d-21-0050.1

NASA Johnson Space Center. (2024). International Space Station (ISS) Earth Observations photography database [Dataset]. *NASA Earth Observations (EOL) Portal*. Retrieved from https://eol.jsc.nasa.gov/SearchPhotos/

NASA/LARC/SD/ASDC. (2024). TEMPO geolocated Earth radiances twilight V03 AuthorAnonymous, (PROVISIONAL) [Dataset]. *NASA Langley Atmospheric Science Data Center DAAC*. https://doi.org/10.5067/IS-40e/TEMPO/RADT_L1.003

Raap, T., Pinxten, R., & Eens, M. (2015). Light pollution disrupts sleep in free-living animals. *Scientific Reports*, *5*(1), 13557. https://doi.org/10.1038/srep13557

Rea, M. S., Figueiro, M. G., Bierman, A., & Hamner, R. (2012). Modelling the spectral sensitivity of the human circadian system. *Lighting Research and Technology*, *44*(4), 386–396. https://doi.org/10.1177/1477153511430474

Román, M. O., Wang, Z., Sun, Q., Kalb, V., Miller, S. D., Molthan, A., et al. (2018a). NASA's Black Marble nighttime lights product suite. *Remote Sensing of Environment*, *210*, 113–143. https://doi.org/10.1016/j.rse.2018.03.017

Román, M. O., Wang, Z., Sun, Q., Kalb, V., Miller, S. D., Molthan, A., et al. (2018b). VIIRS/NPP gap-filled lunar BRDF-Adjusted nighttime lights daily L3 global 500m, v2.0 [Dataset]. In *NASA Level-1 and Atmosphere Archive & Distribution System (LAADS) Distributed Active Archive Center (DAAC)*. Goddard Space Flight Center. https://doi.org/10.5067/VIIRS/VNP46A2.002

Song, J., Wang, J., Xia, X., Lin, R., Wang, Y., Zhou, M., & Fu, D. (2021). Characterization of urban heat Islands using City lights: Insights from MODIS and VIIRS DNB observations. *Remote Sensing*, *13*(16), 3180. https://doi.org/10.3390/rs13163180

Stefani, O., Freyburger, M., Veitz, S., Basishvili, T., Meyer, M., Weibel, J., et al. (2021). Changing color and intensity of LED lighting across the day impacts on circadian melatonin rhythms and sleep in healthy men. *Journal of Pineal Research*, *70*(3), e12714. https://doi.org/10.1111/jpi.12714

Stoken, A., & Fisher, K. (2023). Find my astronaut photo: Automated localization and georectification of astronaut photography. In *Proceedings of the IEEE/CVF conference on computer vision and pattern recognition*.

van Geffen, K. G., van Eck, E., de Boer, R. A., van Grunsven, R. H., Salis, L., Berendse, F., & Veenendaal, E. M. (2015). Artificial light at night inhibits mating in a Geometrid moth. *Insect Conservation and Diversity*, *8*(3), 282–287. https://doi.org/10.1111/icad.12116

Wakefield, A., Stone, E. L., Jones, G., & Harris, S. (2015). Light-emitting diode street lights reduce last-ditch evasive manoeuvres by moths to bat echolocation calls. *Royal Society Open Science*, *2*(8), 150291. https://doi.org/10.1098/rsos.150291

Wang, J., Aegerter, C., Xu, X., & Szykman, J. J. (2016). Potential application of VIIRS Day/Night Band for monitoring nighttime surface PM2. 5 air quality from space. *Atmospheric Environment*, *124*, 55–63. https://doi.org/10.1016/j.atmosenv.2015.11.013

Wang, J., Zhou, M., Xu, X., Roudini, S., Sander, S. P., Pongetti, T. J., et al. (2020). Development of a nighttime shortwave radiative transfer model for remote sensing of nocturnal aerosols and fires from VIIRS. *Remote Sensing of Environment*, *241*, 111727. https://doi.org/10.1016/j.rse.2020.111727

Wang, T., Kaida, N., & Kaida, K. (2023). Effects of outdoor artificial light at night on human health and behavior: A literature review. *Environmental Pollution*, *323*, 121321. https://doi.org/10.1016/j.envpol.2023.121321

Wang, Z., Román, M. O., Kalb, V. L., Miller, S. D., Zhang, J., & Shrestha, R. M. (2021). Quantifying uncertainties in nighttime light retrievals from Suomi-NPP and NOAA-20 VIIRS Day/Night Band data. *Remote Sensing of Environment*, *263*, 112557. https://doi.org/10.1016/j.rse.2021.112557

Xiao, Q., Lyu, Y., Zhou, M., Lu, J., Zhang, K., Wang, J., & Bauer, C. (2023). Artificial light at night and social vulnerability: An environmental justice analysis in the US 2012–2019. *Environment International*, *178*, 108096. https://doi.org/10.1016/j.envint.2023.108096

Xiao, Q., Zhou, M., Lyu, Y., Lu, J., Zhang, K., Figueiro, M., et al. (2023). County-level artificial light at night (ALAN) in the contiguous US (2012–2019): Spatial variations, temporal trends, and environmental justice analyses. *Environmental Science and Pollution Research*, *30*(54), 115870–115881. https://doi.org/10.1007/s11356-023-30572-y

Xue, M. (2026). Background-corrected twilight observation datasets for March 19 case study [Dataset]. *University of Iowa*. https://arroma.uiowa.edu/twilight_observation.php

Zhou, M., Wang, J., Chen, X., Wang, Y., Colarco, P. R., Levy, R. C., & Miller, S. D. (2024). First lunar-light mapping of nighttime dust season oceanic aerosol optical depth over North Atlantic from space. *Remote Sensing of Environment*, *312*, 114315. https://doi.org/10.1016/j.rse.2024.114315

Zhou, M., Wang, J., Chen, X., Xu, X., Colarco, P. R., Miller, S. D., et al. (2021). Nighttime smoke aerosol optical depth over U.S. rural areas: First retrieval from VIIRS moonlight observations. *Remote Sensing of Environment*, *267*, 112717. https://doi.org/10.1016/j.rse.2021.112717

Zhou, M., Wang, J., Garcia, L. C., Chen, X., da Silva, A. M., Wang, Z., et al. (2023). Enhancement of nighttime fire detection and combustion efficiency characterization using Suomi-NPP and NOAA-20 VIIRS instruments. *IEEE Transactions on Geoscience and Remote Sensing*, *61*, 1–20. https://doi.org/10.1109/tgrs.2023.3261664

Zissis, G., Bertoldi, P., & Serrenho, T. (2021). *Update on the Status of LED-Lighting world market since 2018*. Publications Office of the European Union.

Zoogman, P., Liu, X., Suleiman, R., Pennington, W., Flittner, D., Al-Saadi, J., et al. (2017). Tropospheric emissions: Monitoring of pollution (TEMPO). *Journal of quantitative spectroscopy and radiative transfer*, *186*, 17–39. https://doi.org/10.1016/j.jqsrt.2016.05.008